

Transport of ions in a segmented linear Paul trap in printed-circuit-board technology

G Huber¹, T Deuschle, W Schnitzler, R Reichle, K Singer and F Schmidt-Kaler

Institut für Quanteninformationsverarbeitung, Universität Ulm,
Albert-Einstein-Allee 11, D-89069 Ulm, Germany
E-mail: gerhard.huber@uni-ulm.de

New Journal of Physics **10** (2008) 013004 (15pp)

Received 5 October 2007

Published 14 January 2008

Online at <http://www.njp.org/>

doi:10.1088/1367-2630/10/1/013004

Abstract. We describe the construction and operation of a segmented linear Paul trap, fabricated in printed-circuit-board technology with an electrode segment width of $500\ \mu\text{m}$. We prove the applicability of this technology to reliable ion trapping and report the observation of Doppler-cooled ion crystals of $^{40}\text{Ca}^+$ with this kind of trap. Measured trap frequencies agree with numerical simulations at the level of a few percent from which we infer a high fabrication accuracy of the segmented trap. To demonstrate its usefulness and versatility for trapped ion experiments we study the fast transport of a single ion. Our experimental results show a success rate of 99.0(1)% for a transport distance of $2 \times 2\ \text{mm}$ in a round-trip time of $T = 20\ \mu\text{s}$, which corresponds to 4 axial oscillations only. We theoretically and experimentally investigate the excitation of oscillations caused by fast ion transports with error-function voltage ramps: for a slightly slower transport (a round-trip shuttle within $T = 30\ \mu\text{s}$) we observe non-adiabatic motional excitation of 0.89(15) meV.

¹ Author to whom any correspondence should be addressed.

Contents

1. Introduction	2
2. Experimental set-up	3
2.1. Design, fabrication and operation of PCB-traps	3
2.2. Laser excitation and fluorescence detection	4
3. Numerical simulations	5
3.1. Radial confinement	5
3.2. Axial confinement	6
4. Cold ion crystals	6
4.1. Observation of linear crystals and measurement of trap frequencies	6
4.2. Compensation of micromotion	7
5. Transport of single ions and ion crystals	9
5.1. Transport probabilities	12
5.2. Coherent excitation during transport	13
6. Conclusion and outlook	14
Acknowledgments	15
References	15

1. Introduction

Three-dimensional (3D) linear Paul traps are currently used for ion-based quantum computing [1]–[4] and high-precision spectroscopy [5]–[7]. An axial segmentation of the dc electrodes in these traps enables the combination of individual traps to a whole array of micro-traps. Structure sizes down to the range of a few tens of micrometres [8, 9] are nowadays in use and mainly limited by fabrication technology. However, most of these fabrication methods require advanced and non-standard techniques of micro-fabrication as is known from micro-electro-mechanical system (MEMS) processing or advanced laser machining. Long turn-around times and high costs are complicating the progress in ion trap development. In this paper, we present a segmented 3D ion trap which is fabricated in UHV-compatible printed-circuit-board (PCB) technology. While with this technology, spatial dimensions of electrodes are typically limited to more than $100\ \mu\text{m}$, the production of sub-millimetre sized segments is simplified by the commonly used etching process. The advantages of PCB-traps are therefore a fast and reliable fabrication and consequently a quick turn-around time, combined with low fabrication costs. The feasibility of the PCB-technique for trapping ion clouds in a surface-electrode trap has already been shown in [10]. In future, we anticipate enormous impact of the PCB-technology by including standard multi-layer techniques in the trap design. On a longer timescale on-board electronics may be directly included in the layout of the PCB-boards, e.g. digital-to-analog (DA) converters may generate axial trap control voltages or digital radio frequency (RF)-synthesizers could be used for dynamical ion confinement.

In this paper, we first describe the fabrication of our PCB-trap and the overall experimental set-up in section 2. The following section 3 is dedicated to a comparison of measured trap frequencies with numerical simulations for a characterization of radial and axial trapping. Special attention is paid in section 4 to the compensation of electrical charging effects of the

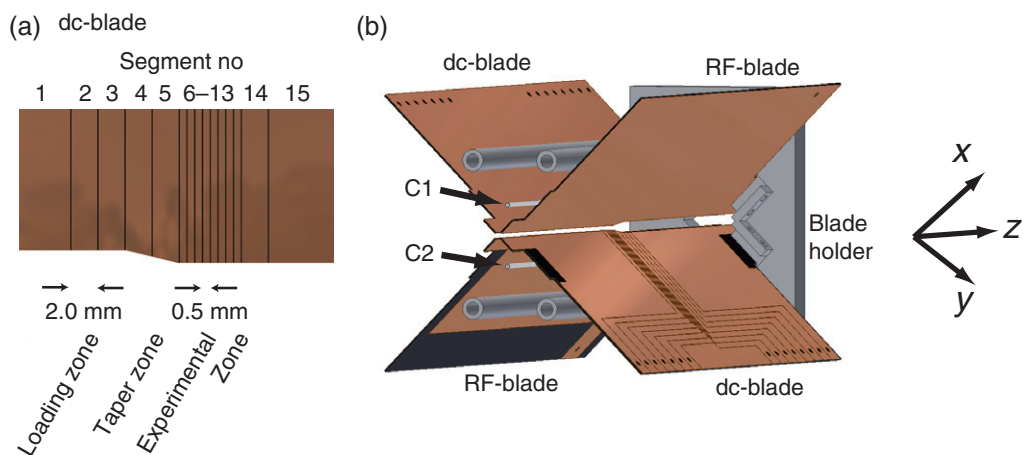


Figure 1. Electrode design. (a) Close-up view of the blade design: the dc-blade segment width is 2 mm in the loading and taper zone, and 0.5 mm in the experimental zone. The trap consists of a 4 mm wide loading zone, a tapered intermediate zone, and a 2 mm wide experimental zone. (b) Sketch of the assembled X-trap consisting of four blades, drawn with missing front blade holder for sake of clarity. Compensation electrodes C1 and C2 are parallel to the trap axis.

trap electrodes since PCB-technology requires insulating grooves between the electrodes that may limit the performance of the trap. We adjust the compensation voltages to cancel the effect of stray charges and investigate the stability of these compensation voltages over a period of months. Our measurements show that PCB-traps are easy to handle, similar to standard linear traps comprising solely metallic electrodes. In section 5, the segmentation of the dc-electrodes is exploited to demonstrate the transport of a single ion, or a small crystal of ions, along twice the distance of 2 mm in a round-trip shuttle over three axial trap segments. Special attention is given to fast transports within total transport times of $T = 20\text{--}100 \mu\text{s}$, corresponding to only 4–20 times the oscillation period of the ion in the potential. We checked the consistency of the measured data with a simple transport model.

2. Experimental set-up

2.1. Design, fabrication and operation of PCB-traps

The trap consists of four blades, two of them are connected to a RF supply and the two remaining, segmented blades are supplied with static (dc) voltages, see figure 1. The dc- and RF-blades are assembled normal to each other (the cross-section is X-shaped). In a loading zone, the two opposing blades are at a distance of 4 mm. A tapered zone is included in order to flatten the potential during a transport between the wider loading and the narrower experimental zone. In the latter zone, the distance between the blades is reduced to 2 mm. The material of the blades is a standard polyimide material coated by $\sim 18 \mu\text{m}$ of copper on all sides of the substrate. Etched insulation grooves of $120 \mu\text{m}$ in the copper define dc-electrodes. The RF-drive frequency near $\Omega/2\pi = 11.81 \text{ MHz}$ is amplified and its amplitude is further increased

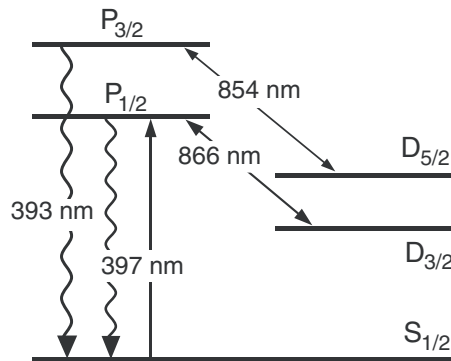


Figure 2. Energy levels and relevant optical transitions of $^{40}\text{Ca}^+$.

by a helical resonator before it is applied to the RF blades. At typical operating conditions, we measure a peak-to-peak voltage of about $V = 400 V_{\text{pp}}$ by using a home-built capacitive divider with a small input capacitance to avoid artificial distortion of the signal by the measurement. The dc-control voltages from a computer card are connected to the trap segments via low-pass RC-filters with corner frequency at 1 MHz. The trap is housed in a stainless steel vacuum chamber with enhanced optical access held by an ion getter and a titanium sublimation pump at a pressure of 3×10^{-10} mbar. This value was reached without bakeout, indicating the UHV-compatibility of the PCB-materials².

2.2. Laser excitation and fluorescence detection

The relevant energy levels of $^{40}\text{Ca}^+$ ions are shown in figure 2. All transitions can be either driven directly by grating stabilized diode lasers, or by frequency doubled diode lasers³. The lasers are locked according to the Pound–Drever–Hall scheme to Zerodur Fabry–Perot cavities for long-term frequency stability. Each laser can quickly be switched on and off by acousto-optical modulators. Optical cooling and detection of resonance fluorescence is achieved by simultaneous application of laser light at 397 and 866 nm. Radiation near 854 nm depopulates the $D_{5/2}$ metastable state (1.2 s lifetime).

Two laser sources at 423 (≤ 5 mW) and 375 nm (≤ 1 mW) are used for photoionization loading of ions [11, 12]. The high loading efficiency allows for a significant reduction of the Ca flux from the resistively heated oven and minimizes the contamination of the trap electrodes. By avoiding the use of electron impact ionization the occurrence of stray charges is greatly suppressed.

In this experiment, laser beams near 397, 866 and 854 nm are superimposed and focused into the trap along two directions: one of these directions (D1) is aligned vertically under 5° with respect to the top–bottom axis and the other beam (D2) enters horizontally and intersects the trap axis under an angle of 45° . A high-NA lens is placed 60 mm from the trap center behind an inverted viewport to monitor the fluorescence of trapped ions at an angle perpendicular to the trap axis direction. The fluorescence light near 397 nm is imaged on to the chip of an EMCCD camera⁴ in order to achieve a photon detection efficiency of about 40%.

² Material P97 by Isola, PCB manufacturer (<http://www.micro-pcb.ch>).

³ Toptica DL100, DL-SHG110 and TA100.

⁴ Electron multiplying CCD camera, Andor iXon DV860-BI.

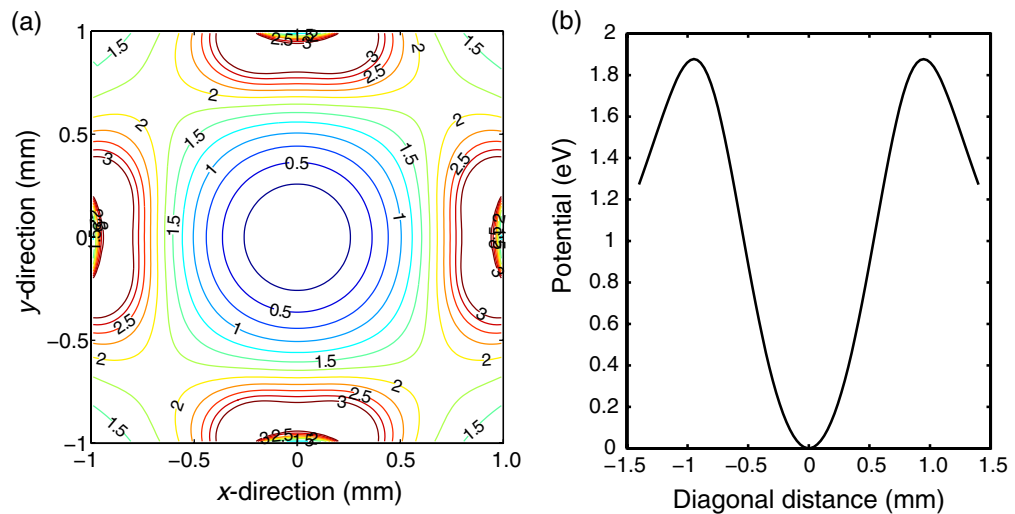


Figure 3. (a) Simulation of the pseudo-potential in the $(x-y)$ -plane in the experimental zone for $V = 408 V_{pp}$. (b) Cross-section through the potential shown in (a) along the $x = y$ -direction yielding a radial trap frequency of $\omega_{rad}/2\pi = 663$ kHz and a trapping depth of approx. 1.9 eV.

3. Numerical simulations

3.1. Radial confinement

The complex layout of the multi-segmented trap requires elaborate numerical techniques to simulate the electrical potentials accurately in order to avoid artificial effects. Instead of using widespread commercial FEM routines that mesh the whole volume between the electrodes, boundary-element methods (BEM) are more suited but also more complex in their implementation. The effort in such methods is reduced for large-space computations since they only need to mesh surfaces of nearby electrodes and multipole approximations are done to include far distant segments in order to speed up computations. We have written a framework for the solution of multipole-accelerated Laplace problems⁵. This method is not limited in the number of meshed areas and thus allows for accurate calculations with a fine mesh. In the simulations presented here, we typically subdivide the surfaces of the trap electrodes into approx. 29 000 plane areas to determine the charge distributions and the free-space potential within the trap volume numerically. Figure 3(a) shows the calculated pseudo-potential in the $(x-y)$ -plane of the experimental zone for a RF of $\Omega/2\pi = 11.81$ MHz and a RF peak-to-peak voltage $V = 408 V_{pp}$. By symmetry the diagonal directions along $x = \pm y$ contain the nearest local maximum and thus determine the relevant trap depth of approx. 1.9 eV for the applied experimental parameters. A cross-section through the pseudo-potential along this direction is shown in figure 3(b) at the same axial position as in figure 3(a). From these simulations, we are able to extract a radial trap frequency of $\omega_{rad}/2\pi = 663$ kHz in the absence of applied dc potentials.

⁵ The solver was developed by the MIT Computational Prototyping Group (<http://www.rle.mit.edu/cpg>).

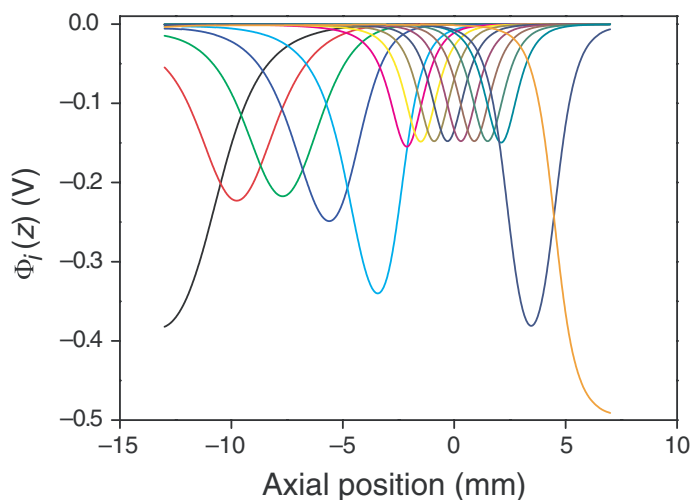


Figure 4. Individual axial electrode pair potentials $\phi_i(z)$. For detailed description see text in section 3.2. Narrow electrodes show a lower maximum potential due to the smaller amount of surface charges. An arbitrary axial potential is formed by superposing individual contributions.

3.2. Axial confinement

For axial confinement opposing dc electrodes are set to the same voltage U_i , $i = 1, \dots, 15$ labeling the electrode number as depicted in figure 1. These voltages are supplied by DA converters covering a voltage range of ± 10 V with a maximum update rate of 1 MHz. Figure 4 illustrates the potentials $\phi_i(z)$ obtained when only U_i is set to -1 V and all other voltages are set to zero. For arbitrary voltage configurations, the axial potential $\phi(z) = \sum_i U_i \phi_i(z)$ is a linear superposition of the single electrode potentials. Tailored axial potentials for the generation of single or multiple axial wells with given secular frequency, depth and position of the potential minimum are obtained by solving the linear equation given above for the voltages U_i . Time-dependent voltages are used to move the potential minimum guiding the trapped ion along the trap axis.

4. Cold ion crystals

4.1. Observation of linear crystals and measurement of trap frequencies

The trap is operated in the loading configuration with dc voltages of $U_{\text{load}} = \{\dots, U_7, \dots, U_{13}, \dots\}_{t=0} = \{\dots, 6 \text{ V}, \dots, 8 \text{ V}, \dots\}$ while non-specified segment voltages are held at ground potential. From simulations we estimate that the axial trap frequency is $\omega_z/2\pi = 199$ kHz at the potential minimum close to the center of electrode 10. Linear strings and single ions crystallize under continuous Doppler cooling with beams D1 and D2, consisting of superimposed beams at 397 (0.3 mW with $60 \mu\text{m}$ beam waist), 866 and 854 nm (both 3 mW with $100 \mu\text{m}$ beam waist), cf figure 5.

Applying a sinusoidal waveform with 1 mV amplitude to electrode segment 10 allows for a parametrical excitation near resonance. Observation of the ion excitation through decreasing fluorescence on the EMCCD image signifies a resonance condition. This way,

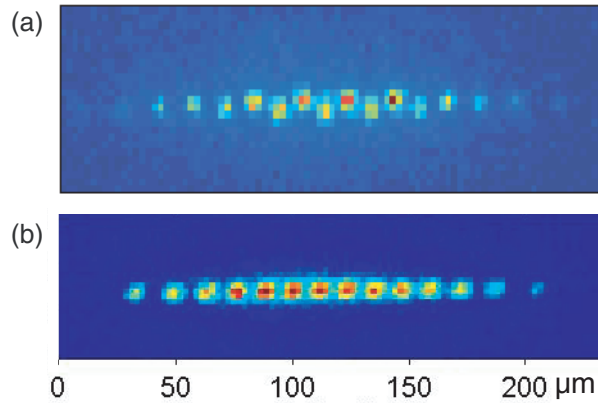


Figure 5. (a) Fluorescence of an ion crystal with 14 ions in a zig-zag configuration as observed with the EMCCD camera. Exposure time was set to 100 ms (optical magnification is 10.4). (b) Linear crystal with 14 ions and a slightly more relaxed axial trap frequency than in (a). This induces a phase transition into a purely linear configuration of ion positions.

we experimentally find a radial frequency of $\omega_{\text{rad}}/2\pi = 700(2)$ kHz and an axial frequency of $\omega_z/2\pi = 191(2)$ kHz. We attribute the 5% deviations to residual electric fields arising mainly from charging of the etched insulation groove cuts as well as to the limited accuracy of the RF-voltage amplitude measurement. Stable trapping at a q -value of about 0.16 is achieved. Measuring the mutual distances in a linear two- or three-ion crystal easily allows for calibrating the optical magnification of the imaging optics to be 10.4, with a CCD-pixel size of $24 \mu\text{m}$. For determining the resonant frequency of the cycling transition used for Doppler cooling the fluorescence is detected on a photomultiplier tube (PMT) while scanning the laser frequency at 397 and/or 866 nm. This yields an asymmetric line profile of about 30–50 MHz FWHM, exhibiting the features of a dark resonance with a maximum count rate of 20 kHz. For all following measurements we keep the detuning of the 397 nm laser at $\Gamma/2$ (half of the linewidth) fixed and adjust the frequency of the 866 nm laser to obtain a maximum fluorescence rate.

4.2. Compensation of micromotion

Ions in small traps are likely to be affected by stray charges that shift the ions out of the RF null since those charges can often not be neglected in most ion traps. Therefore, the dynamics of ions in general exhibits a driven micromotion oscillation at a frequency of $\Omega/2\pi$ leading to a broadening of the Doppler cooling transition and higher motional excitation [13]. A second disadvantage of micromotion is a reduced photon scattering rate at the ideal laser detuning of $\Gamma/2$. To correct for potentials induced by stray charges and maybe geometric imperfections we can apply compensation voltages to the electrodes labeled C1 and C2, as sketched in figure 1(b).

For detecting the micromotion we trigger a counter with a photon event measured by the PMT in the experimental zone and stop the counter by a TTL phase locked to half the trap drive frequency $\Omega/2\pi$. If the ion undergoes driven motion, the fluorescence rate is modulated as a cause of a modulated Doppler line shape, see figure 6(a). Here, we detect the ion motion

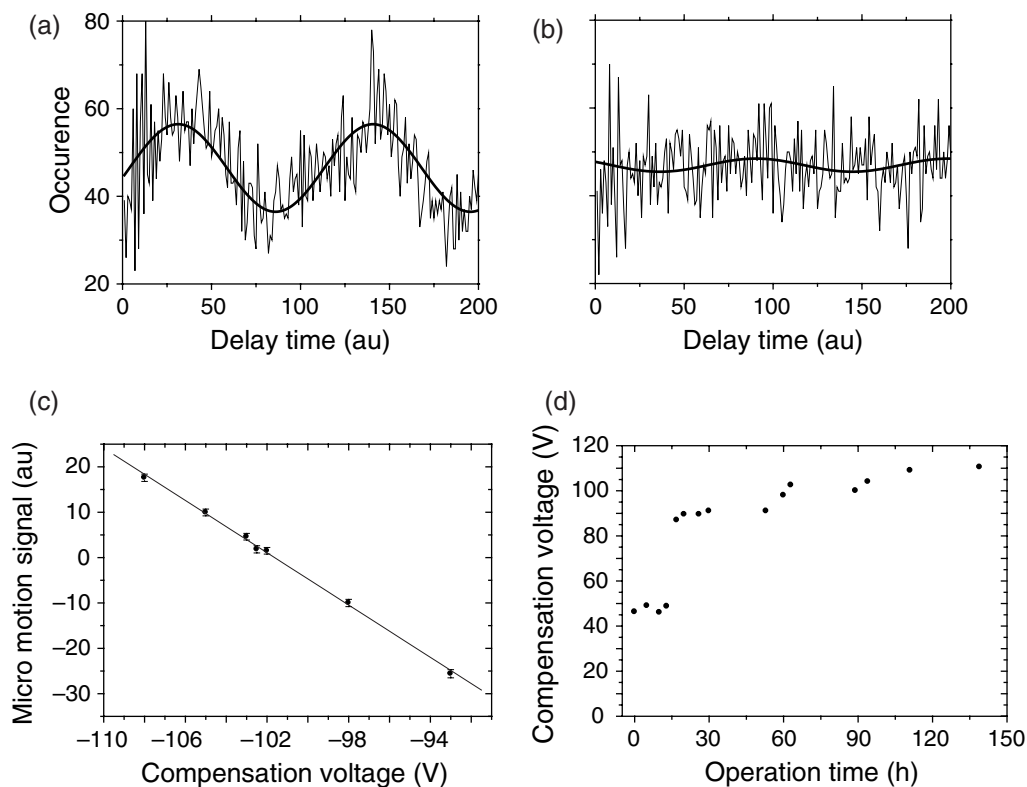


Figure 6. Histogram of photon count events for different values of micromotion compensation voltages: (a) Trace far from compensation with $U_{C1} = 98$ V fitted to a sine function. (b) Near to optimum compensation with $U_{C1} = 102.5$ V. (c) The amplitude of a sinusoidal fit for different compensation voltages shows a linear dependence between the amplitude and applied compensation. Negative amplitudes correspond to a 180° phase flip; this happens when the ion passes the RF null. A linear fit reveals the optimal value at $U_{C1} = 101.6$ V. With this data an optimal compensation is determined within an uncertainty of less than 0.3 V. The overall data collection time is less than 5 min. (d) Optimum compensation voltage plotted versus the operation time of the oven. We attribute the long-term drift of this voltage to an increasing calcium contamination on the trap electrodes in the experimental zone.

in the direction of the laser beam. If a flat histogram is measured the ion does not possess a correlated motion with the RF driving voltage. Then, it resides close to the RF null where the modulation vanishes, cf figure 6(b). From taking a series of histograms for different values of the compensation voltage a linear relation between observed modulation and applied compensation is obtained. The optimal compensation voltage can then be read from the abscissa for zero correlation amplitude, figure 6(c).

Our long-term observation of the optimum compensation voltage indicates a weak increase over three months. Since we did not bakeout the vacuum chamber, storage times of ions are several minutes so that we needed to reload ions from time to time. During all experimental sessions, we kept the temperature of the oven fixed so that the flux of neutral Ca atoms was

sustained. This is not necessary in a better vacuum environment. An oven current of 7 A leads to a flux such that we reach a high loading rate of 0.1–0.4 ions per second. Thus, by operating the oven continuously we could accumulate a long operation time of over 150 h. The 20% step in figure 6(d) was caused by a power failure.

By comparing our measurements to the long-term recording of [14] for a 2 mm linear trap [15] with stainless steel electrodes we find similar drifts in compensation voltages. Thus, it seems that PCB-traps can be corrected equally well for micromotion so that the larger insulation grooves do not harm the performance.

In all of the experiments presented here the beam of neutral calcium is directed into the narrow experimental zone where micromotion is compensated as described above. In future, however, we plan to use the loading zone where a higher loading rate through the larger involved phase space during trapping is expected. Then, ions can be shuttled into the cleaner experimental zone 8 mm apart. Calcium contamination will then be completely avoided and much lower compensation voltages and drifts are expected. The segmented PCB-trap operated this way may even show an improved micromotion compensation stability as compared to traditional linear and 3D traps having less insulation exposed to the ions.

5. Transport of single ions and ion crystals

As recently suggested [16], ions in a future quantum computer based on a segmented linear Paul trap might be even shuttled through stationary laser beams to enable gate interactions. In a different approach, one might shuttle ions between the quantum logic operations [17]. This would alleviate more complex algorithms and reduce the enormous technological requirements extensively. According to theoretical investigations [18], transport could occupy up to 95% of operation time in realistic algorithms. Given the limited coherence time for qubits, shuttling times need therefore to be minimized. Our work as described below may be seen in the context of the theoretical and experimental works found in [19]–[21]. With our multi-segmented Paul trap, we have made first investigations of these speed limits in order to enter the non-adiabatic regime and studied the corresponding energy transfer. Preferred transport ramps are theoretically well understood [22]. The current challenge arises from experimental issues, i.e. how accurate potentials can be supplied, how drifts in potentials can be avoided and whether sophisticated shuttling protocols can be used [23]. First transport studies have been made some years ago by the Boulder group using an extremely sparse electrode array [24]. Non-adiabatic transports of cold neutral atom clouds in a dipole trap have been demonstrated in [25] and show very similar qualitative behavior, even though on a completely different timescale (axial frequency of approx. $2\pi \times 8$ Hz).

The PCB-trap described here contains 15 pairs of dc-segments. Using a suitable time sequence of control voltages $U_i(t)$, $i = 1, \dots, 15$, the axial potential can be shaped time-dependently in a way to transport ions along the trap axis. In the following, we present the results of various transport functions for a distance of $2d = 4$ mm.

For these measurements, we follow a six-step sequence:

- 1) Initially, we confine an ion in an axial trapping potential in the loading configuration U_{load} , figure 7(a). The single ion is laser cooled by radiation near 397 and 866 nm. Compensation voltages have previously been optimized for this trap configuration such that the width of the excitation resonance near 397 nm is minimal. Then, the laser beams are switched off.

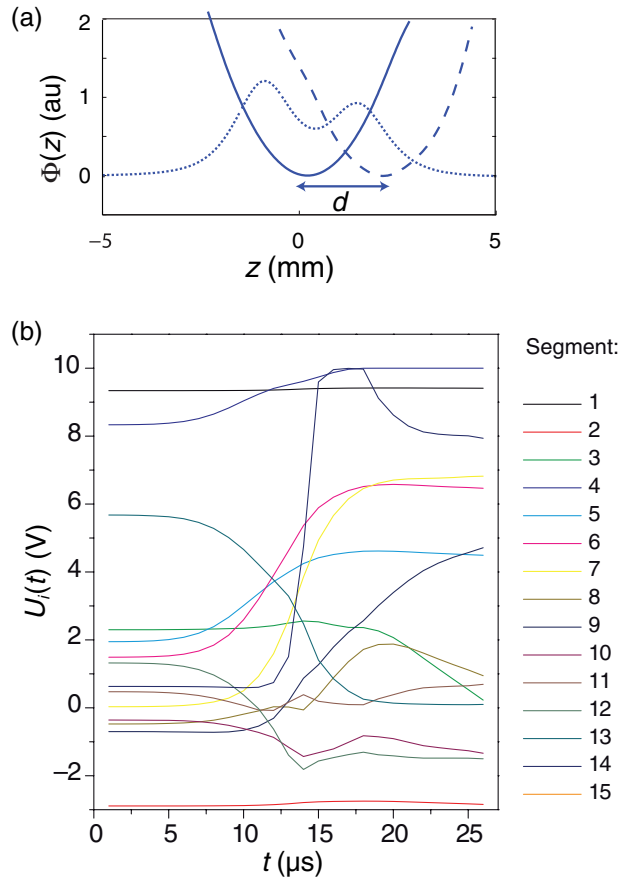


Figure 7. (a) Axial potentials for loading and observing ions (dotted line) U_{load} , at the beginning (solid line) of the transport with $U_{\text{trans}}(t = 0) = \{-8.77, 9.34, -2.89, 2.30, 8.33, 1.95, 1.49, 0.03, -0.48, -0.70, -0.36, 0.47, 1.32, 5.68, 0.63\}$ V and at its turning point (dashed line). (b) Trap control voltages U_1 to U_{15} for transporting the ion by an error function ramp. Discontinuities in the curves result from the time discretization in steps of $1 \mu\text{s}$.

- 2) Before starting the transport, U_{load} is linearly changed into the initial transport potential $U_{\text{trans}}(t = 0)$ in 10 steps each taking $1 \mu\text{s}$. Note that the transport potential should be adapted in shape and depth, and is not necessarily identical to the optimum potential for laser excitation, for fluorescence observation, and for quantum logic gate operations. In our case, the axial trap frequency for $U_{\text{trans}}(t = 0)$ is adjusted for $\omega_z/2\pi = 200 \text{ kHz}$, and the minimum positions of U_{load} and U_{trans} both coincide with the center of segment 10. The voltages for the transport potential are chosen according to the regularization of [22].
- 3) By changing the control voltages such that the potential minimum of U_{trans} moves according to an error function, the ion is accelerated and moved to a turning point 2 mm away, centered roughly above segment 13.
- 4) The ion is accelerated back to the starting point again using the same time-inverted waveforms. By our calculations, we aim to determine the control voltages such that the ion always remains within a harmonic potential well of constant frequency ω_z throughout the whole transport procedure.

- 5) Finally, the transport potential U_{trans} is ramped back linearly in $10\ \mu\text{s}$ into the initial potential U_{load} .
- 6) The laser radiation is switched on again to investigate either the success probability of the transport or the motional excitation of the ion.

The sequence is repeated about 10^3 – 10^5 times, then the parameters of the transport ramp in step (3) and (4) are changed and the scheme is repeated.

Ideally, we would create an axial potential that closely approximates $\phi(z, t) = m\omega_z^2(z - z_0(t))^2/2q$ with an explicit time-dependent position of the potential minimum $z_0(t)$. However, all presented simulations and motional excitation energies were deduced from the numerical axial potentials instead. Moving the potential minimum from its starting point $z_0(0) = 0$ to the turning point $z_0(T/2) = 2\ \text{mm}$ and back again to $z_0(T) = 0$ leads to a drag on the trapped ion. For sake of convenience, we express the total time for a round-trip T in units of the trap period $\tau \equiv T\omega_z/2\pi$. The dimensionless parameter τ then denotes the number of oscillations the ion undergoes in the harmonic well during the transport time. The functional form of the time-dependent position of the potential minimum $z_0(t)$ is crucial for the transport success and the motional excitation. We have chosen a truncated error-function according to

$$f_\sigma(t) = \frac{d}{2} \left(1 + \frac{\text{Erf}[(4t/T - 1)\sigma]}{\text{Erf}[\sigma]} \right), \quad z_0(t) = \begin{cases} f_\sigma(t), & 0 \leq t \leq T/2, \\ d - f_\sigma(T - t), & T/2 < t \leq T, \end{cases} \quad (1)$$

as input to find the waveforms of all contributing electrode pairs, figure 7(b).

Small first and second derivatives at the corner points assure that the ion experiences only smoothly varying accelerations at these times. The parameter σ determines the maximum slope of the function. The smoother the shuttling begins the higher average and maximum velocities are needed for a fast transport. A high maximum velocity \dot{z}_0 results in far excursions of the ion from the potential minimum so that it may experience higher derivatives not fulfilling the harmonic potential approximation anymore. A compromise can be found between slowly varying corner point conditions and ion excitation due to fast, non-adiabatic potential movements. Experimentally, we found the lowest energy accumulated for $\sigma = 2.3$. In our experiment, the update time of the supply hardware for the electrode voltages is limited to $1\ \mu\text{s}$. To account for this effect in our simulations we also discretize $z_0(t)$ in time steps. These discontinuities are evident in figure 7(b) already indicating that a higher sampling rate of the DA channels would be desirable. Furthermore, for short shuttles the amplitude discretization through the DA converters makes an exact reproduction of $z_0(t)$ impossible. This gives rise to discrete dragging forces transferring motional excess energy to the ion. We verified by numerical simulations that even for the fastest transports with durations of only $T \approx 10$ – $12\ \mu\text{s}$, deviations from the non-discretized time evolution were negligible. Since in our case, the typical involved motional energies are much larger than $\hbar\omega$, a simple classical and one-dimensional model of the ion transport is justified with the equation of motion

$$\ddot{z}(t) = -\frac{q}{m} \frac{d\phi(z, t)}{dz} = -\omega^2(z - z_0(t))^2. \quad (2)$$

We solve this equation numerically for functions $z_0(t)$ with varying σ . The resulting phase space trajectories $\{z(t), \dot{z}(t)\}$ are plotted in figure 8 for $T = 20\ \mu\text{s}$ ($\tau = 4$) and $T = 16\ \mu\text{s}$ ($\tau = 3.2$). In the first case, the phase space trajectory starts and ends close to $\{0,0\}$, i.e. both the potential and the kinetic energy are modest after the transport. In the second case, the particle reaches

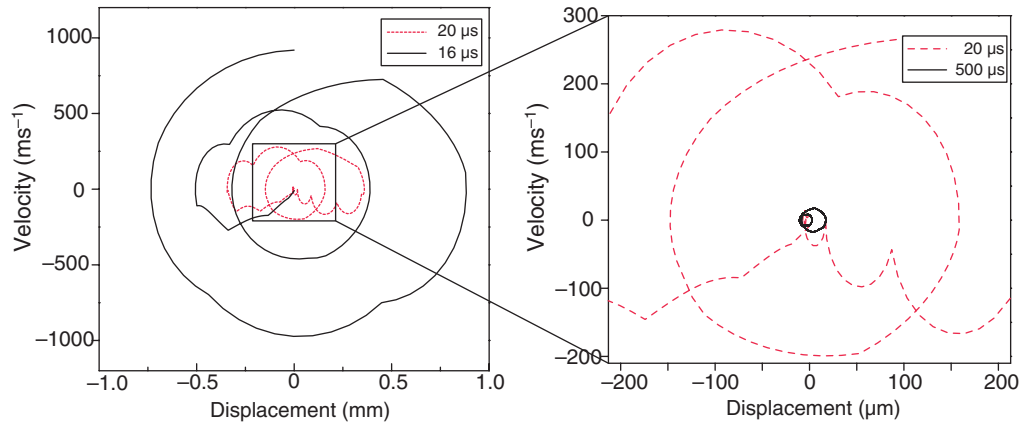


Figure 8. Phase space trajectories of an ion for two different transport durations. The closed loop (dotted line, $\tau = 4$) indicates a transport with low final motional energy. For $\tau = 3.2$ (dashed line) the ion does not reach zero velocity at $t = T$ and a final energy of 171 meV. Discontinuities in the trajectories result from the time discretization in steps of $1 \mu\text{s}$.

its starting point $z_0(T) = z(0)$ again, but resides with a high oscillating velocity $\dot{z}(T)$ but small displacement.

5.1. Transport probabilities

This section addresses the question of how fast the transport of an ion in the manner described above can eventually be performed before it gets lost. In the following, we discuss transports in the adiabatic regime $\tau \gg 1$ and far off this regime. For the measurements, an experimental sequence with transport duration τ is interleaved by Doppler cooling cycles of 1 s duration to ensure to start always from the same initial energy close to the Doppler limit. After n_i successful transports with $i = 1, \dots, N$, the ion may finally be lost. After 100–1000 repetitions, we bin the data into a histogram of n_i approximating the success probability $P_\tau(n)$ that allows for deduction of the fraction of ions having performed at least n successful transports. $P_\tau(n)$ is fitted to an exponential decay introducing the single transport success probability \tilde{p}_τ , $P_\tau(n) = (\tilde{p}_\tau)^n$. The probability for n successful transports equals $(\tilde{p}_\tau)^n$ as the processes are independent with a sufficiently long Doppler cooling period. To account for other sources of ion loss, e.g. from background gas collisions, a loss rate without transport in sequence steps (3) and (4) was subtracted. These losses can be modeled by introducing a second decay channel in $P_\tau(n)$ to finally yield net transport probabilities p_τ .

Figure 9 depicts values p_τ for different transport durations τ performed with a transport function $z_0(t)$ according to equation (1) with $\sigma = 2$. In the adiabatic regime, we obtain a success probability of 99.8% for $\tau = 100$. The ion stays deep within the potential well guaranteeing low losses. This is in good agreement with theoretical predictions. The very high success probability stays almost constant within the adiabatic regime down to $\tau = 4$ ($p_4 = 99.0\%$). According to our model, the ion experiences a relative displacement of over $300 \mu\text{m}$ gaining a potential energy of more than 30 meV. Even faster transports lead to higher transport losses resulting in probabilities around 85%. When the energy of the ion exceeds about 30% of the depth of the potential, we observe a strongly increased loss probability.

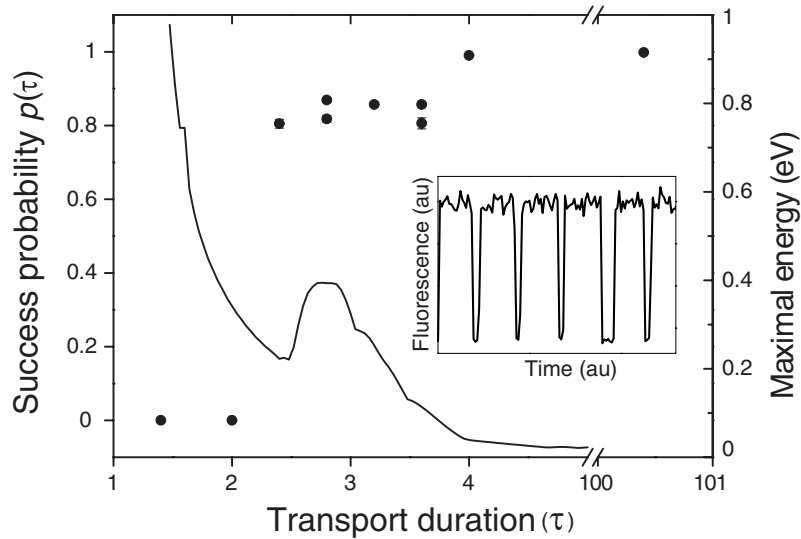


Figure 9. Transport success probability as a function of transport time (dots), y-scale on left. Slow transports with large τ show a success probability close to unity. In the intermediate range $2.5 \leq \tau \leq 4$, the probability reduces to approx. 85%. From the model we deduce the ion's maximum energy during the transport (solid), y-scale on right side. Inset: fluorescence level as observed by the CCD camera showing the dark periods during the transport while the bright periods indicate a successful transport.

5.2. Coherent excitation during transport

If the ions are to be laser-cooled after a fast shuttle, it is important to keep the excitation of vibrational degrees of freedom minimal. Therefore, we quantitatively investigate the ion's kinetic energy after the transport for ramps in the non-adiabatic regime with $4 < \tau \leq 20$. We generalize a method which was recently employed [26, 27] to measure motional heating rates in a micro-ion trap.

After a transport, in step (6) of the experimental sequence, the oscillating ion is Doppler-cooled by laser light, and scatters an increasing amount of photons as it cools down. We observe the scattered photons by a PMT as a function of time. The scattering rate in our model depends on the laser power quantified by a saturation parameter s , the laser detuning Δ , and the motional energy of the ion. In contrary to [26] we do not average over a thermal state. For large excitations, the oscillation amplitude exceeds the waist of the cooling laser resulting in a low scattering rate. A uniform laser intensity is therefore not appropriate for describing our experiments. We take this effect into account by including a Gaussian beam waist of $w_0 = 60 \mu\text{m}$ in our simulations. The efficiency of the laser cooling sets in with a sharp rise of PMT counts shortly after t_{recover} . Only then, the scattering rate reaches its steady state value at the Doppler-cooling limit, see figure 10(a). Adapting the theoretical treatment for a thermal motional state in [26] to the case of a coherent motional oscillation [27] and including a spatial laser beam profile, the recovery time of fluorescence is quantitatively identified with the energy after the transport. The results are shown in figure 10(b) and compared to the theoretical simulations of our simple classical model. As expected, the motional excitation

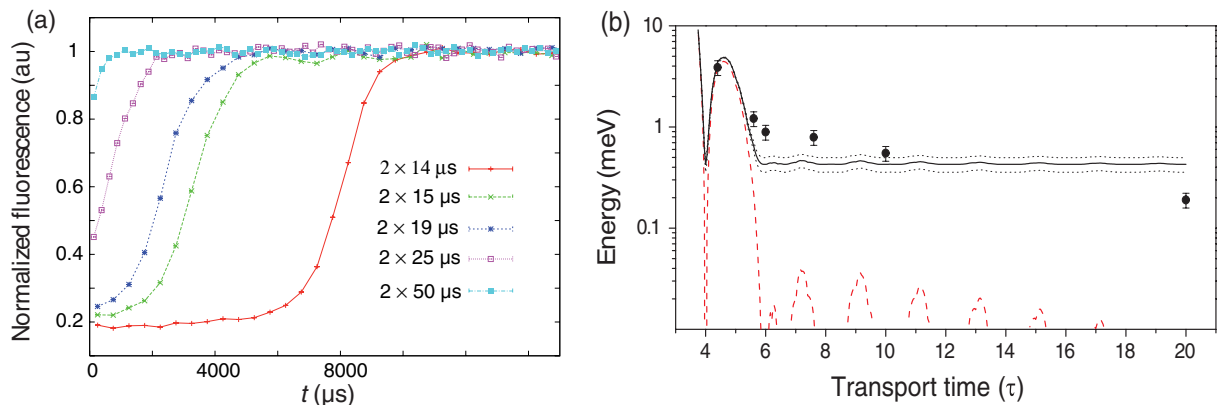


Figure 10. (a) Fluorescence rate after the transport and during application of Doppler cooling. Fast transport results in large excitation and a late recovery of the fluorescence level from vibrational excitation. (b) Measured excitation energy after an error function transport with $\tau = 4\text{--}20$. Error bars of the data points account for the uncertainty of the excitation energy from the photon scattering rate, taking into account uncertainties in the laser beam waist $60(10) \mu\text{m}$, laser saturation uncertainty of 15%, and laser detuning uncertainty of 30 MHz. The overall uncertainty results in 15% errors for the excitation energy. The theoretical prediction of the simple model (dashed line) for solely the error function transport does not agree with the data. However, we found a motional excitation of $0.427(73) \text{ meV}$ due to the morphing steps of the potential before and after the transport by replacing steps (3) and (4) in the measurement cycle by a waiting time of equal length. The solid line shows this modified prediction together with its standard deviation (dotted).

increases for short transport times τ . For slow transports, i.e. $\tau \gg 1$, the excitation does not drop below a certain threshold. We found that this excess excitation is due to the morphing steps (2) and (5) and might be caused by a non-ideal matching of the respective potential minima. Even a few micrometres difference leads to a large kick during the linear morphing ramp. We measured this effect independently by replacing steps (3) and (4) by equal waiting times without voltage ramps. Corrected for this excess heating, the model agrees well with the measured data.

The motional heating rate omitting any transport or morphing steps has been measured independently for our trap by replacing steps (2)–(4) by waiting times of 500 and 2000 ms. We deduce an energy gain of $3(1) \text{ meV s}^{-1}$. During our transport cycles this increase in energy only amounts to about $1.5 \mu\text{eV}$. This minor energy gain does not affect our measurement results and conclusions on the transport-induced excitation.

6. Conclusion and outlook

Employing a novel segmented linear Paul trap, we demonstrated stable trapping of single ions and cold ion crystals. For the first time we have shown fast, non-adiabatic transports over $2 \times 2 \text{ mm}$ travels within a few microseconds by error function ramps. The main achievement

is the characterization of the ion's motional excitation. The method is based on the measured modification of the ion's scattering rate during Doppler cooling. In the future, however, sideband cooling and spectroscopic sideband analysis will be applied yielding a much more sensitive tool to investigate motional energy transfers. This will lead to a largely improved determination of ion excess motion. Then subtle changes of the parameters and the application of optimal control theory for the voltage ramps may be applied to yield lower motional excitation. Furthermore, we will establish a dedicated loading zone and optimize the transport of single ions and linear crystals through the tapered zone.

For micro-structured segmented ion traps with axial trap frequencies of several megahertz, the application of the demonstrated techniques will lead to transport times of a few microseconds only. This way, future quantum algorithms may no longer be limited by the ion transport but only by the time required for logic gate operations.

Acknowledgments

We acknowledge financial support by the Landesstiftung Baden-Württemberg, the Deutsche Forschungsgemeinschaft within the SFB-TR21, the European Commission and the European Union under the contract no. MRTN-CT-2006-035369 (EMALI).

References

- [1] Wineland D J *et al* 2005 *Proc. 17th Int. Conf. on Laser Spectroscopy* (Singapore: World Scientific) p 393
- [2] Becher C *et al* 2005 *Proc. 17th Int. Conf. on Laser Spectroscopy* (Singapore: World Scientific) p 381
- [3] Barrett M D *et al* 2004 *Nature* **429** 737
- [4] Riebe M *et al* 2004 *Nature* **429** 734
- [5] Schmidt P O *et al* 2005 *Science* **309** 749
- [6] Rosenband T *et al* 2007 *Phys. Rev. Lett.* **98** 220801
- [7] Roos C F *et al* 2006 *Nature* **443** 316
- [8] Stick D *et al* 2006 *Nat. Phys.* **2** 36
- [9] Seidelin S *et al* 2006 *Phys. Rev. Lett.* **96** 253003
- [10] Brown K R *et al* 2007 *Phys. Rev. A* **75** 015401
- [11] Gulde S *et al* 2001 *Appl. Phys. B* **73** 861
- [12] Kjaergaard N *et al* 2000 *Appl. Phys. B* **71** 207
- [13] Berkeland D J *et al* 1998 *J. Appl. Phys.* **83** 5025
- [14] Rotter D 2003 *Diploma Thesis* Universität Innsbruck
- [15] Schmidt-Kaler F *et al* 2003 *Appl. Phys. B* **77** 789
- [16] Leibfried D, Knill E, Ospelkaus C and Wineland D J 2007 *Phys. Rev. A* **76** 032324
- [17] Kielpinski D, Monroe C and Wineland D J 2002 *Nature* **417** 709
- [18] Chuang I 2006 private communication
- [19] Home J P *et al* 2006 *Quantum Inf. Comput.* **6** 289
- [20] Hucul D *et al* 2007 *Preprint* [quant-ph/0702175v2](http://arxiv.org/abs/quant-ph/0702175v2)
- [21] Hensinger W K *et al* 2006 *Appl. Phys. Lett.* **88** 034101
- [22] Reichle R *et al* 2006 *Fortschr. Phys.* **54** 666
- [23] Schulz S, Poschinger U, Singer K and Schmidt-Kaler F 2006 *Fortschr. Phys.* **54** 648
- [24] Rowe M A *et al* 2002 *Quantum Inf. Comput.* **2** 257
- [25] Couvert A *et al* 2007 *Preprint* [0708.4197v1](http://arxiv.org/abs/0708.4197v1)
- [26] Wesenberg J H *et al* 2007 *Preprint* [0707.1314](http://arxiv.org/abs/0707.1314)
- [27] Reichle R *et al* in preparation